

Date of publication, date of current version.

Digital Object Identifier

# Analysis of an improved circuit for laser chaos and its synchronisation

R. Concas<sup>1</sup>, A. Montori<sup>2,4</sup>, E. Pugliese<sup>5</sup>, A. Perinelli<sup>6,7</sup>, L. Ricci<sup>6,8</sup> (Member, IEEE), and R. Meucci<sup>3,5</sup> (Senior Member, IEEE)

<sup>1</sup>Istituto Nazionale di Ricerca Metrologica (INRiM), 10135 Torino, Italy

<sup>2</sup>European Laboratory for Nonlinear Spectroscopy (LENS), 50019 Sesto Fiorentino, Italy

<sup>3</sup>Department of Physics, University of Florence (UNIFI), 50019 Sesto Fiorentino, Italy

<sup>4</sup>Istituto Nazionale di Ottica (CNR-INO), 50019 Sesto Fiorentino, Italy

<sup>5</sup>Istituto Nazionale di Ottica (CNR-INO), Largo E. Fermi 6, 50125 Firenze, Italy

<sup>6</sup>Department of Physics, University of Trento, Italy

<sup>7</sup>TIFPA-INFN, University of Trento, Italy

<sup>8</sup>CIMeC (Center for Mind/Brain Sciences), University of Trento, Italy

Corresponding author: Roberto Concas (e-mail: r.concas@inrim.it)

This work was supported by the Project 20FUN01 TSCAC, which has received funding from the EMPIR programme co-financed by the Participating States and from the European Union's Horizon 2020 research and innovation programme. Open Access Funding provided by Istituto Nazionale di Ricerca Metrologica within the CARE-CRUI Agreement.

**ABSTRACT** The exploration of chaos, synchronization, and circuit implementation in analog simulations unveils a versatile framework with diverse applications. Originating from a universal chaos model rooted in laser physics, its adaptability extends to neural dynamics and random number generation, where both rely on characteristic time scales. Circuit implementations using op-amps and analog multipliers offer tangible avenues for exploration. However, challenges like bias and trajectory distortion drive the need for innovative solutions. Through numerical integration and circuit simulations, analysis of chaotic regimes such as Sub-harmonic Chaos (SC) and Homoclinic Chaos (HC) reveals crucial behaviors for applications like secure communications. Despite experimental hurdles, advancements in circuit design promise novel pathways for chaos synchronization studies. Understanding the intricate interplay between chaos and these systems is vital, given their reliance on characteristic time scales. Additionally, exploring chaos synchronization, especially within analog circuits, shows potential for revolutionizing information processing capabilities, despite inherent challenges. Progress in circuit design persists, forging new avenues in chaos synchronization studies, shaping a dynamic landscape poised for further exploration and innovation.

**INDEX TERMS** Analog simulations, chaos, chaos synchronisation, circuit design.

## I. INTRODUCTION

THE minimal universal model for chaos [1]–[3] has its origins in the physics of a laser subjected to a feedback that controls its losses via a simple low-pass filter with an appropriate cut-off frequency [4].

However, the potential of this model is not limited to laser physics. This is because the relaxation rates of the three variables describing the system's evolution can be changed in very large intervals. For example, when dynamics occurs on time scales of the order of hundreds of milliseconds, the model shows interesting overlaps with the dynamics of neurons [5]. This is the case when a sub-threshold electrical activity of a neuron is interrupted by high amplitude pulses thus signaling action-potentials. The model can be easily controlled by relying on a suitably chosen control frequency [6].

Furthermore, if the dynamics is driven to higher frequencies, the model was shown to be well-suited for applications in the field of random number generation [7], which is crucial for data transfer or storage and secure communications [8], [9].

The paper is organized as follows: in Sec. II the circuit design is described, starting from the analysis of the differential equations underlying the model to the description of the proposed circuital implementation; in Sec. III the numerical and electronic simulations are presented along with the related analysis of the result in both the sub-harmonic bifurcation type regime and the homoclinic one; in Sec. IV the analysis of the synchronisation between two independent circuits is discussed; in the concluding section we summarize and provide some outlook.

**II. MINIMAL UNIVERSAL OSCILLATOR MODEL AND CIRCUIT DESIGN**

**A. MODEL EQUATIONS**

The minimal universal laser model is described by the following system of first-order differential equations:

$$\frac{dx}{dt} = -k_0 (x + k_1 x z^2 - xy), \tag{1a}$$

$$\frac{dy}{dt} = -\gamma (y + xy - p_0), \tag{1b}$$

$$\frac{dz}{dt} = -\beta (z - B_0 + B_1 x). \tag{1c}$$

In these equations:  $x$  is the “fast” variable that represents the laser output intensity and has a typical unperturbed decay rate  $k_0 = 2 \cdot 10^7 \text{ s}^{-1}$ ;  $y$  is the “slow” variable that represents the population inversion with pumping rate  $\gamma p_0$  and has a typical decay rate  $\gamma = 10^5 \text{ s}^{-1}$ ;  $z$  is the “intermediate” feedback variable, which affects  $x$  in a nonlinear way (see the term  $xz^2$  in the first equation) even if it is regulated in a linear way via a low-pass filter. This filter, characterized by a typical bandwidth  $\beta = 10^6 \text{ s}^{-1}$ , is fed by the fast variable  $x$ , properly amplified by the factor  $B_1$ , along with a bias  $B_0$ .

It is interesting to note that the time evolution of the system can be modified without altering its dynamics, and thus the related phase portraits, by scaling the three rates  $k, \gamma, \beta$  by the same factor  $\alpha$ : if the rates are divided by  $\alpha$ , and  $\alpha > 1$  ( $\alpha < 1$ ), the dynamics is slowed (accelerated) by a factor  $\alpha$ , as setting  $\tau = \alpha t$  leaves Eqs. (1) unchanged.

In the following, this property was exploited to implement an electronic simulation of Eqs. (1) and thus to cope with the limited bandwidth response introduced by the analog electronic components: setting  $\alpha = 10^3$ , the typical values mentioned above for the three rates become

$$k'_0 = \frac{k_0}{10^3} = 2 \cdot 10^4 \text{ s}^{-1},$$

$$\gamma' = \frac{\gamma}{10^3} = 10^2 \text{ s}^{-1},$$

$$\beta' = \frac{\beta}{10^3} = 10^3 \text{ s}^{-1},$$

Consequently, the evolution becomes  $10^3$  times slower, as the system of equations gets

$$\frac{dx}{d\tau} = -k'_0 (x + k_1 x z^2 - xy), \tag{2a}$$

$$\frac{dy}{d\tau} = -\gamma' (y + xy - p_0), \tag{2b}$$

$$\frac{dz}{d\tau} = -\beta' (z - B_0 + B_1 x), \tag{2c}$$

where

$$\tau = 10^3 t.$$

**B. CIRCUIT DESCRIPTION**

The system of differential equations describing the minimal universal laser model can be solved via analog computation by using a suitable combination of integrated circuits, namely op-amps and analog multipliers, and passive electronic components.

As mentioned in the Introduction, the implementation proposed by Ricci *et al.* [2] is affected by issues leading to the presence of an undesired bias term and the unwanted distortion of the trajectory in phase space. The circuit proposed here provides an elegant and effective solution to these problems.

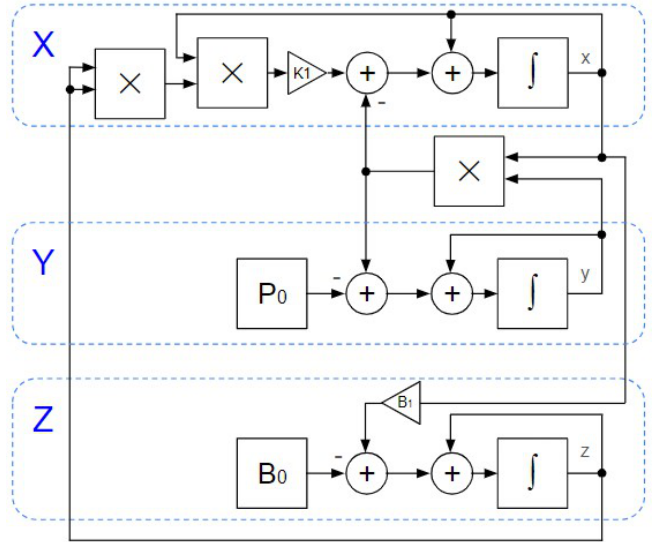


FIGURE 1: Design block of the implementation of the minimal universal model. The architecture consists of three functional blocks X, Y, Z, each enclosed by a blue, dashed line, that implement the differential equations providing  $x, y, z$ .

The design block shown in Fig. 1 relies on three multipliers and three summing integrators, which produce the outputs  $x, y, z$  and are characterized by the time constant  $\tau_X, \tau_Y, \tau_Z$ , respectively. The circuit implementation of this architecture is shown in Fig. 2. All active components are assumed to be power supplied with  $\pm 15 \text{ V}$ .

The nonlinear terms are obtained by using three identical blocks, each containing an analog multiplier AD633JN and a noninverting amplifier based on the operational amplifier (op-amp) AD820. Given the five multiplier inputs  $\hat{X}, \hat{X}_0, \hat{Y}, \hat{Y}_0, \hat{Z}_0$ , the output  $\hat{W}$  of the analog multiplier AD633JN is given by

$$\hat{W} = \frac{1}{V_0} (\hat{X} - \hat{X}_0)(\hat{Y} - \hat{Y}_0) + \hat{Z}_0,$$

where  $V_0 = 10 \text{ V}$ . In the present implementation,  $\hat{X}_0 = \hat{Y}_0 = \hat{Z}_0 = 0$ . The output  $\hat{W}$  is then amplified by a factor 10 due to  $R_i = 1 \text{ k}\Omega, R_f = 9 \text{ k}\Omega$ . Consequently, given the inputs  $A, B$ , each nonlinear block generates an output  $C$  given by

$$C = \frac{A \cdot B}{1 \text{ V}}.$$

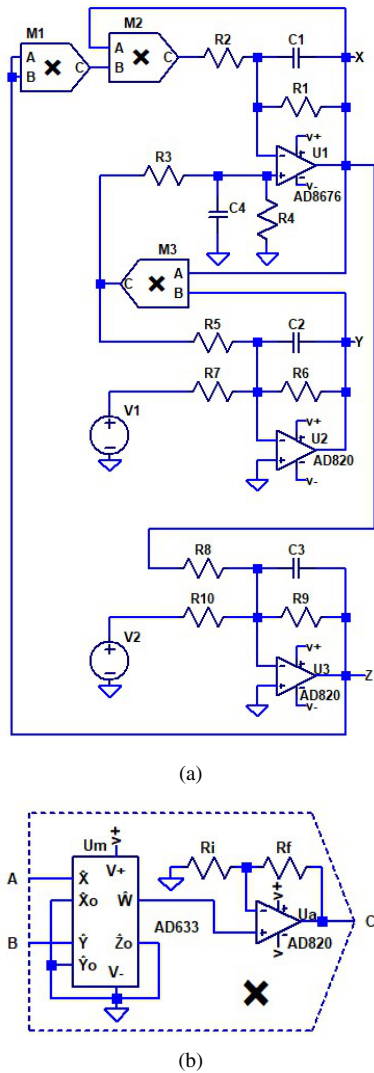


FIGURE 2: (a) Schematic of the circuit implementing the minimal universal model. (b) Structure of a single nonlinear block, having two input ports  $A, B$  and an output port  $C$ .

The integrator producing  $y$  is based on the op-amp AD820 and is fed with the terms  $V_1, xy, y$ . (The one producing  $x$  is described below.) In the frequency domain, we have

$$-\frac{s}{\gamma'} \tilde{y} = \tilde{y} + \frac{R_6}{R_5} \tilde{x}\tilde{y} - p_0$$

where

$$\gamma' = (R_6 C_2)^{-1}. \quad (3a)$$

$$p_0 = -\frac{R_6}{R_7} V_1. \quad (3b)$$

By setting

$$R_5 = R_6, \quad (4)$$

the block producing  $y$  turns out to implement Eq. (2b).

The integrator producing  $z$  is based on the op-amp AD820 and is fed with the terms  $V_2, x$  and  $z$ . In the frequency domain, we have

$$-\frac{s}{\beta'} \tilde{z} = \tilde{z} - B_0 + B_1 \tilde{x}$$

where

$$\beta' = (R_9 C_3)^{-1}. \quad (5a)$$

$$B_1 = \frac{R_9}{R_8}, \quad (5b)$$

$$B_0 = -\frac{R_9}{R_{10}} V_2. \quad (5c)$$

In this way the block producing  $z$  turns out to implement Eq. (2c) directly.

The integrator producing  $x$  is based on the op-amp AD8676 and is fed with the terms  $xz^2, xy, x$ . By using a standard analysis in the Laplace frequency domain the output of the op-amp is given by

$$-\frac{s}{k'_0} \tilde{x} = \tilde{x} + k'_1 \tilde{x}\tilde{z}^2 - k_2(s) \tilde{x}\tilde{y}$$

where  $s = j\omega$ ,  $\tilde{A}$  represent the Laplace transforms of a generic time-dependent quantity  $A$ , and

$$k'_0 = (R_1 C_1)^{-1}, \quad (6a)$$

$$k'_1 = \frac{R_1}{R_2}. \quad (6b)$$

The introduced factor  $k_2(s)$  is defined as:

$$k_2(s) = \frac{R_4}{R_2} \frac{R_1 + R_2(1 + sR_1 C_1)}{R_4 + R_3(1 + sR_4 C_4)} \quad (7)$$

It is straightforward to show that  $k_2(s) = 1$  independently of  $s$  if

$$\frac{R_3}{R_4} = \frac{R_1}{R_2}, \quad (8a)$$

$$C_4 = C_1 \frac{R_1}{R_3}. \quad (8b)$$

Consequently, by complying with these two conditions, the block producing  $x$  turns out to implement Eq. (2a), as it can be promptly verified by inverting the previous equation in the frequency domain  $s$ .

The chosen implementation of the differential equation for  $x$  shows different advantages compared with previous solutions [1], [2]. First, the contribution  $xy$  being fed into the noninverting input of  $U_1$  via a carefully trimmed network (see Eq. (8b) above), allows to save an op-amp to generate the sign inversion of  $xy$ . However, the possibly most important improvement consists in the suppression of bias effects that, for example, had to be compensated for in the implementation discussed by Ricci et al. [2] via a manual adjustment of two trimmers.

### III. SIMULATION AND ANALYSIS OF CHAOS

The analysis of the proposed design is carried out with two different approaches: numerical integration and circuit simulation. The results of the comparison between the numerical integration of the model described by Eqs. (1) and the circuit simulation based on the electronic scheme of Fig. 2 and described by Eqs.(2) is summarised in Fig. 3.

As mentioned above, two chaotic regimes are considered. The first one, referred to as Sub-harmonic Chaos (SC), is a

chaotic regime obtained after sub-harmonic bifurcations of a limit cycle originated from a Hopf bifurcation. The second regime is named Homoclinic Chaos (HC) and is characterised by pulses of the same height but erratically separated in time due to the re-injection mechanism around the local chaos SC. The re-injection mechanism is provided by the stationary solution of Eqs. (1) with zero intensity.

### A. NUMERICAL INTEGRATION

A numerical integration of Eqs (1) was performed by using Berkeley Madonna software and relying on the built-in Runge-Kutta 4th order integrator with an integration step of  $0.1 \mu\text{s}$ . The fixed parameter values are:

$$k_0 = 2 \cdot 10^7 \text{ s}^{-1}, \quad \gamma = 10^5 \text{ s}^{-1}, \quad \beta = 10^6 \text{ s}^{-1}, \\ k_1 = 33, \quad B_1 = 0.222, \quad p_0 = 1.4.$$

The two chaotic regimes are obtained by setting the adjustable parameter  $B_0$  as follows:

$$B_0 = \begin{cases} 0.0938, & \text{for SC.} \\ 0.0941, & \text{for HC.} \end{cases}$$

The resulting phase portraits in the  $x-z$  space and the related  $x$  time series are shown in Figs. 3a, 3c, 3e, 3g.

### B. SPICE SIMULATION

The analog electronic simulation was carried out by using the software spice-based LTSpice<sup>®</sup>, which allows to reliably simulate analog or digital electronic circuits by means of models of electronic components used therein. This type of electronic simulation can consider nonidealities and limits of the components and it reproduces the full electronic behavior of op-amps and multipliers such as output voltage dynamic, input offset voltage, slew rate, multiplier's non-linearity. Consequently, simulations mostly faithfully reproduce what would result from real implementations.

Considering the design of Fig. 2, embedded spice models were used for both the passive components and the op-amps, whereas a basic spice model for multipliers was chosen. Once the boundary conditions are assigned, and neglecting a transient of 0.5 s, the simulation covers a span of 5 s.

The chosen nominal values of the passive components are listed in Table (1).

	Value (k $\Omega$ )		Value (k $\Omega$ )		Value (nF)
R1	33	R6	10	C1	1.5
R2	1	R7	10	C2	1000
R3	330	R8	4.5	C3	1000
R4	10	R9	1	C4	0.15
R5	10	R10	1		

TABLE 1: Nominal values set for the passive components.

The choice complies with the constraints set by Eqs. (8a), (8b), (4).

According to Eqs. (6a), (3a), (5a), the resulting time constants are:

$$k'_0 = 2.02 \cdot 10^4 \text{ s}^{-1}, \quad \gamma' = 10^2 \text{ s}^{-1}, \quad \beta' = 10^3 \text{ s}^{-1}.$$

Similarly, according to Eqs. (6b), (5b), the parameters  $k_1, B_1$  are given by

$$k_1 = 33, \quad B_1 = 0.222,$$

whereas, according to Eqs. (3b), (5c), the parameters  $p_0, B_0$  are given by

$$p_0 = -V_1(\text{V}), \quad B_0 = -V_2(\text{V}).$$

Finally, the tunable voltage parameters are

$$V_1 = -1.4 \text{ V} \Rightarrow p_0 = 1.4,$$

and the two chaotic regimes are obtained by setting

$$V_2 \begin{cases} -0.0956 \text{ V} \Rightarrow B_0 = 0.0956, & \text{for SC.} \\ -0.0946 \text{ V} \Rightarrow B_0 = 0.0946, & \text{for HC.} \end{cases}$$

The results of the electronic simulation results are displayed in Figs. 3b, 3d, 3f, 3h.

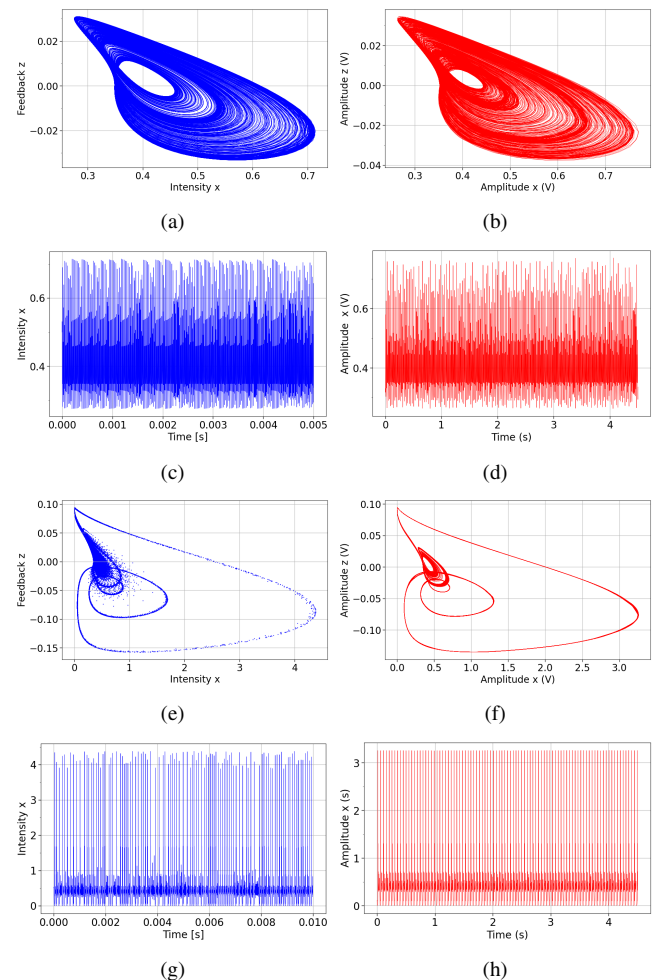


FIGURE 3: Numerical integration of Eqs.(1) (left panels): a) SC attractor in phase space  $x-z$ ; c) SC time series of the variable  $x$ ; e) HC attractor in phase space  $x-z$ ; g) HC time series of the variable  $x$ . Spice simulation of Eqs.(2) (right panels): b) SC attractor in phase space  $x-z$ ; d) SC time series of the variable  $x$ ; f) HC attractor in phase space  $x-z$ ; h) HC time series of the variable  $x$ .



Figures 3 point at a remarkable similarity between the numerical integration and the spice simulation results. Figure. 3f highlights the predicted advantage of the architecture when HC is considered: the slightly squared-off trajectory for the variable  $x$  it is no more present as in previous implementations [1], [2]. Due to the presence of the additional amplification following the multipliers (see Fig. 2), the dynamics is kept within the output voltage swing of the op-amps and consequently it prevents the saturation for the output voltages close to the power supply voltage.

### C. EVIDENCE OF A CHAOTIC BEHAVIOR

An interesting point concerns the evidence of a chaotic behavior hinted at by the shape of the attractors shown in Fig. 3. Finding the evidence of chaos is a nontrivial task, especially when one has to rely on scalar time series. Although chaos can be shown to exist by knowing the nonlinear differential equations underlying a system and thereupon evaluating the Lyapunov spectrum via the so-called standard method [10], [11], in compliance with the approach followed in the present work, here we carried out an analysis on the time series stemming from the numerical simulations.

To look for chaos, we followed an approach [12] that relies on: first, the assessment of the correlation dimension on a “lattice” [13] of embedding pairs  $(m, L)$ , where  $m, L$  are the dimension and the lag of the embedding, respectively; second, the identification of a hyperbolae-bounded region in which the correlation dimension is essentially constant and larger than 2; the evaluation of the maximum Lyapunov exponent (MLE) by using the “divergence rate method” [14], [15].

The “chasing chaos” protocol outlined above was carried out on a time series made of  $2.5 \cdot 10^5$  points corresponding to the variable  $X$  and resulting from the numerical integration described in Sec. III-A. The correlation dimension was evaluated by using a recently-developed method [16] on a lattice of 380 embedding  $(m, L)$  points, where  $2 \leq m \leq 20$ ,  $1 \leq L \leq 20$ . The diagram in Fig. 4 (a) shows the results of the evaluation. Figure 4 (b) shows the plot of the evaluated correlation dimension  $\hat{\nu}$  as a function of the embedding window  $(m-1)L$ . A horizontal straight line fit to the 15 black points within the interval  $110 \geq (m-1)L \geq 200$  provides  $\hat{\nu} = 2.25 \pm 0.01$  and a reduced  $\chi^2$  of 0.86.

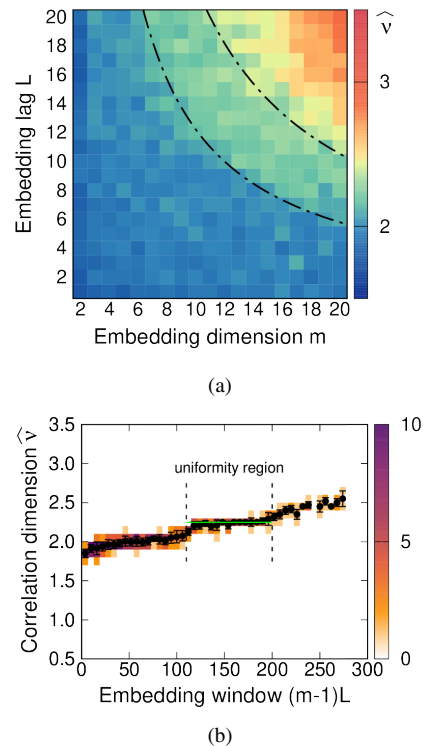


FIGURE 4: (a) Color map of the estimated correlation dimension  $\hat{\nu}$  on the embedding lattice  $2 \leq m \leq 20$ ,  $1 \leq L \leq 20$ . The dash-dotted lines represent the two hyperbolae  $(m-1)L = 110$ ,  $(m-1)L = 200$  that bound the uniformity region. (b) Estimated correlation dimension  $\hat{\nu}$  as a function of the embedding windows  $(m-1)L$ . The color map represents the joint histogram of  $\hat{\nu}$ ,  $(m-1)L$ , built with a bin size of 0.1 and 6, respectively. The black dots and errorbars correspond to the average and standard deviation, respectively, of each marginal histogram at a given embedding window. The uniformity region highlighted in (a) corresponds to the embedding-window-independent behavior of  $\hat{\nu}$  between the embedding window values 110, 200. The green segment corresponds to the best-fit horizontal straight line at  $\hat{\nu} = 2.25$ .

The embedding pairs belonging to the uniformity region for the correlation dimension are expected to provide reliable embedding choices for the evaluation of the MLE too [12], [15]. As mentioned above, this evaluation was carried out by means of the divergence rate method. The results are shown in Fig. 5: the estimated MLE is  $(23 \pm 1) \text{ ms}^{-1}$ .

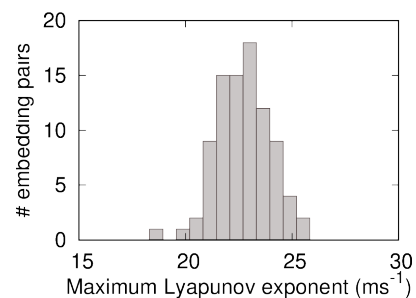


FIGURE 5: Histogram of the MLE computed on the embedding pairs belonging to the uniformity region.

#### IV. SYNCHRONISATION BETWEEN CIRCUITS

Synchronization of chaotic behavior in coupled lasers has become a hot issue since the seminal paper on chaos synchronization by Pecora and Carroll in 1990 [17].

Synchronization emerges as a consequence of the addition of a forcing term to the systems or by suitably coupling them [18]. The emergence of synchronization phenomena is interesting for information processing processes, in order to achieve high-rate and secure communications [19], [20]. More recently, synchronization in a network of dynamical systems where the connected oscillators become transceiver nodes was investigated [21].

Chaos synchronization between two lasers has been experimentally confirmed in solid state lasers [22], CO<sub>2</sub> lasers [23], and semiconductor lasers [24], [25]. Synchronization of globally coupled identical modulated laser models via the linear and nonlinear forms of diffusive couplings was also recently investigated [26].

Synchronization between two circuits of the kind discussed by Ricci *et al.* [2] failed to be experimentally observed, despite a strong evidence relying on numerical simulations [3]. A plausible explanation concerns the spurious biases in the circuitual block generating the variable  $x$  that are avoided in the improved design discussed in the present paper.

#### A. SYNCHRONISATION ARCHITECTURE

By operating suitable minor changes, the scheme shown in Fig. 2 is suitable to study synchronisation among chaotic systems. For the sake of simplicity, we focus the attention on the synchronisation between two chaotic systems.

From a general point of view, we can suppose  $W$  as the output of a generic unit and  $S$  as the synchronisation input for the unit. In the case of a laser,  $W$  corresponds to the laser output intensity  $x$ . Usually the “population inversion” variable  $y$  in a laser is physically inaccessible. As a consequence, it is reasonable to perturb the system via the feedback variable  $z$ , so  $S$  becomes the reference signal on which the synchronisation error is built as  $\varepsilon(S - W)$ , where  $\varepsilon$  represents the coupling strength.

Let us now consider the bidirectional coupling between two laser units as in Fig. 6 by means of the following synchronisation error equations:

$$\varepsilon(S_1 - W_1) = \varepsilon(x_2 - x_1), \quad (9a)$$

$$\varepsilon(S_2 - W_2) = \varepsilon(x_1 - x_2), \quad (9b)$$

where  $x_1$  is the laser output intensity of the unit of interest and  $x_2$  is the laser output intensity provided by the other unit.

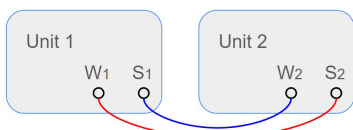


FIGURE 6: Coupling scheme for synchronisation between two laser units.  $W_1$  and  $W_2$  are the output of the units,  $S_1$  and  $S_2$  are synchronisation input.

Equations (9) represent the perturbation to be added as linear term to the feedback equation (1c). The dynamic behavior of two bidirectional coupled laser system becomes:

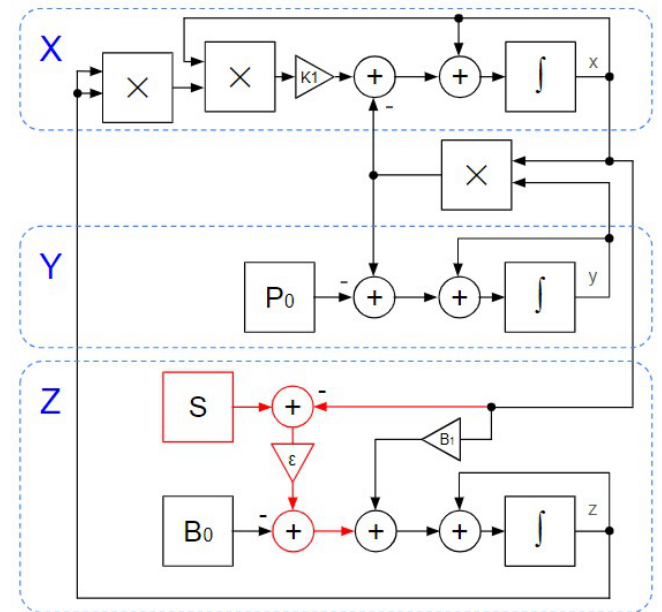
$$\frac{dz_1}{dt} = -\beta [z_1 - B_0 + B_1x + \varepsilon(x_2 - x_1)], \quad (10a)$$

$$\frac{dz_2}{dt} = -\beta [z_2 - B_0 + B_1x + \varepsilon(x_1 - x_2)]. \quad (10b)$$

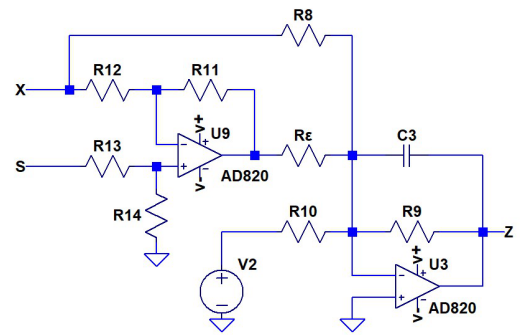
For the sake of simplicity, the equations for the laser units (i.e. laser intensity  $x_1$  and  $x_2$ , and population inversion  $y_1$  and  $y_2$ ) are not reported in Eqs. (10).

#### B. CIRCUIT DESCRIPTION

The coupling dynamics can be implemented in the electrical scheme shown in Fig. 7:



(a)



(b)

FIGURE 7: (a) Design block for synchronisation; changes with respect to the single oscillator implementation are highlighted in red. (b) Circuitual implementation (block Z).

The functional block  $Z$ , shown in Fig. 7a contains an additional summing node in which the synchronisation error

is applied. The circuitual implementation is shown in Fig. 7b, where the difference term in Eqs.(9) is evaluated by using an additional op-amp AD820 in differential configuration: the signal  $x$  is connected to the inverting input and corresponds to the signal  $x_1$ ; the signal  $s$  is connected to the noninverting input and corresponds to the signal  $x_2$ . Considering the condition

$$\frac{R_{11}}{R_{12}} = \frac{R_{14}}{R_{13}}$$

the differential output signal is given by

$$\hat{Z} = \frac{R_{11}}{R_{12}} (S - W) = \frac{R_{11}}{R_{12}} (x_2 - x_1)$$

By setting

$$R_{11} = R_{12} = R_{13} = R_{14} = 10 \text{ k}\Omega$$

the gain of the differential stage is unitary. It follows

$$\hat{Z} = (x_2 - x_1).$$

The resistor  $R_\varepsilon$  allows to adjust the coupling strength as

$$\varepsilon = \frac{R_9}{R_\varepsilon}. \quad (11)$$

According to Eqs. (10), (11), the system of equations for the bidirectional coupling implementation becomes:

$$\begin{aligned} -\frac{s}{(R_9 C_3)} \tilde{z}_1 &= \tilde{z}_1 + \frac{R_9}{R_{10}} V_2 + \frac{R_9}{R_8} \tilde{x}_1 + \frac{R_9}{R_\varepsilon} (\tilde{x}_2 - \tilde{x}_1) \quad , \\ -\frac{s}{(R_9 C_3)} \tilde{z}_2 &= \tilde{z}_2 + \frac{R_9}{R_{10}} V_2 + \frac{R_9}{R_8} \tilde{x}_2 + \frac{R_9}{R_\varepsilon} (\tilde{x}_1 - \tilde{x}_2) \quad . \end{aligned}$$

### C. SIMULATION

The fixed and tunable parameter values used in Sec. III-A for the numerical integration and in Sec. III-B for the Spice simulation are also used for synchronisation analysis.

The numerical integration analysis was carried out with the following settings of  $\varepsilon$

$$\varepsilon \begin{cases} 0 & \text{for SC} \\ 0.128 & \\ 0.168 & \end{cases} \quad \varepsilon \begin{cases} 0 & \text{for HC} \\ 0.128 & \\ 0.168 & \end{cases}$$

The Spice simulation analysis was performed with the following settings of  $R_\varepsilon$ :

$$R_\varepsilon \begin{cases} 1 \text{ M}\Omega & \Rightarrow \varepsilon = 0.001 \\ 10 \text{ k}\Omega & \Rightarrow \varepsilon = 0.1 \\ 1 \text{ k}\Omega & \Rightarrow \varepsilon = 1 \end{cases} \quad R_\varepsilon \begin{cases} 1 \text{ M}\Omega & \Rightarrow \varepsilon = 0.001 \\ 10 \text{ k}\Omega & \Rightarrow \varepsilon = 0.1 \\ 1 \text{ k}\Omega & \Rightarrow \varepsilon = 1 \end{cases}$$

where  $R_\varepsilon = 1 \text{ M}\Omega$  is the minimum resistance value that ensures the ‘‘no coupling’’ condition.

Numerical integration has limited resources for coupling system analysis with elevate coupling strength whenever  $\varepsilon > 0.2$ . Conversely, the electronic simulation allows to test the synchronised system with larger values of correspondent  $\varepsilon$  by decreasing the resistor  $R_\varepsilon$ .

The comparison between numerical integration and Spice simulation is displayed in Fig. 8.

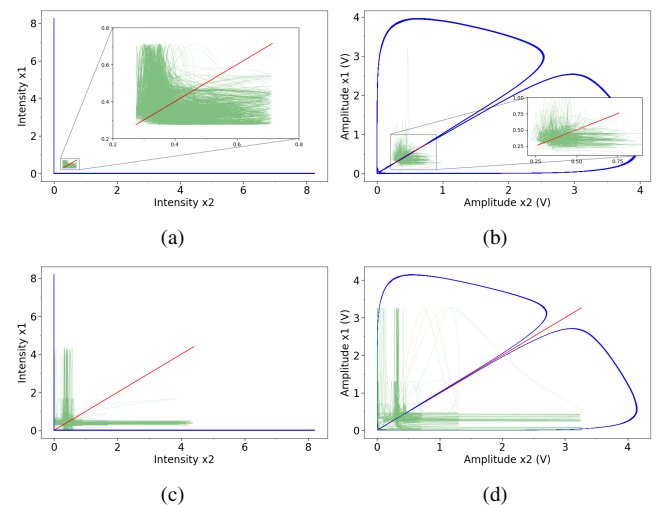


FIGURE 8: Synchronisation of chaos as a function of coupling strength  $\varepsilon$ . Numerical integration (left panels): (a) synchronisation of SC in phase space  $x_1$ - $x_2$ ; (c) synchronisation of HC in phase space  $x_1$ - $x_2$ . Spice simulation (right panels): (b) synchronisation of SC in phase space  $x_1$ - $x_2$ ; (d) synchronisation of HC in phase space  $x_1$ - $x_2$ .

Figures 8a and 8c show synchronisation results (numerical integration) in SC and HC regimes for the three chosen coupling strength values: green color refers to  $\varepsilon = 0$  (no coupling); red color to  $\varepsilon = 0.128$  (full synchronisation); blue color refers to  $\varepsilon = 0.168$  (periodic synchronisation).

Figures 8b and 8d show synchronisation results obtained via Spice simulation in both SC and HC regimes for the three chosen  $R_\varepsilon$  corresponding to coupling strength values: green color refers to  $R_\varepsilon = 1 \text{ M}\Omega$  (no coupling); red color to  $R_\varepsilon = 10 \text{ k}\Omega$  (full synchronisation); blue color to  $R_\varepsilon = 1 \text{ k}\Omega$  (periodic synchronisation).

As the coupling strength  $\varepsilon$  increases, in both SC and HC regimes, the full synchronisation of chaos is suddenly transformed in a new periodic synchronisation regime (anti-phase synchronisation) characterised by high laser intensity amplitudes  $x_1$  and  $x_2$ , as shown in Fig. 9.

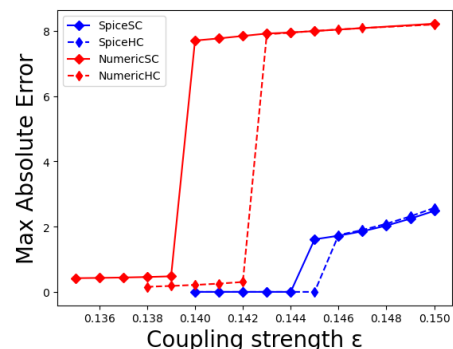


FIGURE 9: Maximum error as a function of the coupling strength  $\varepsilon$  at the transition from full synchronisation to explosive periodic synchronisation.

This transition is an evidence of explosive synchronisation as investigated by Boccaletti *et al.* [27].

## V. CONCLUSIONS

The circuitual implementation of the minimal universal laser model has been improved by simplifying the topology and removing the saturation effects of electronic devices. Because simulations with two different approaches return equivalent results, the circuitual scheme is mature for new network implementations. In this framework, a bidirectional coupling scheme for studying the synchronisation in two different chaotic regimes is proposed. In both cases, the full synchronisation evolves toward an explosive synchronisation regime that is relevant for different research fields.

## REFERENCES

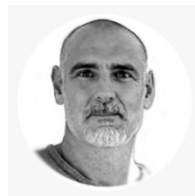
- [1] R. Meucci, S. Euzzor, F. T. Arecchi, and J.-M. Ginoux, "Minimal universal model for chaos in laser with feedback," *International Journal of Bifurcation and Chaos*, vol. 31, p. 2130013, mar 2021.
- [2] L. Ricci, A. Perinelli, M. Castelluzzo, S. Euzzor, and R. Meucci, "Experimental evidence of chaos generated by a minimal universal oscillator model," *International Journal of Bifurcation and Chaos*, vol. 31, no. 12, p. 2150205, 2021.
- [3] M. Castelluzzo, M. Cescato, L. Ricci, R. Meucci, and A. Perinelli, "Experimental implementation of a laser model with cavity loss modulation," in *2022 IEEE Workshop on Complexity in Engineering (COMPENG)*, pp. 1–5, 2022.
- [4] F. T. Arecchi, W. Gadamski, and R. Meucci, "Generation of chaotic dynamics by feedback on a laser," *Phys. Rev. A*, vol. 34, pp. 1617–1620, Aug 1986.
- [5] F. Arecchi, "Chaotic neuron dynamics, synchronization and feature binding," *Physica A: Statistical Mechanics and its Applications*, vol. 338, no. 1, pp. 218–237, 2004. Proceedings of the conference A Nonlinear World: the Real World, 2nd International Conference on Frontier Science.
- [6] E. Allaria, F. T. Arecchi, A. Di Garbo, and R. Meucci, "Synchronization of homoclinic chaos," *Phys. Rev. Lett.*, vol. 86, pp. 791–794, Jan 2001.
- [7] B. Shi, C. Luo, J. G. F. Flores, G. Lo, D.-L. Kwong, J. Wu, and C. W. Wong, "Gbps physical random bit generation based on the mesoscopic chaos of a silicon photonics crystal microcavity," *Opt. Express*, vol. 28, pp. 36685–36695, Nov 2020.
- [8] R. Guo, M. Li, X. Liu, and Z. Wei, "Research on space laser hybrid chaotic shift keying secure communication system," in *2020 International Conference on Wireless Communications and Smart Grid (ICWCSG)*, (Los Alamitos, CA, USA), pp. 14–17, IEEE Computer Society, jun 2020.
- [9] X. Liu, R. Guo, M. Li, and Z. Wei, "Research on image encryption in secure communication system of space laser chaos keying," in *2020 International Conference on Wireless Communications and Smart Grid (ICWCSG)*, (Los Alamitos, CA, USA), pp. 10–13, IEEE Computer Society, jun 2020.
- [10] G. Benettin, L. Galgani, A. Giorgilli, and J. Strelcyn, "Lyapunov characteristic exponents for smooth dynamical systems and for Hamiltonian systems; a method for computing all of them. Part 1: Theory," *Meccanica*, vol. 15, pp. 9–20, 1980.
- [11] G. Benettin, L. Galgani, A. Giorgilli, and J. Strelcyn, "Lyapunov characteristic exponents for smooth dynamical systems and for Hamiltonian systems; a method for computing all of them. Part 2: Numerical application," *Meccanica*, vol. 15, pp. 21–30, 1980.
- [12] A. Perinelli and L. Ricci, "Chasing chaos by improved identification of suitable embedding dimensions and lags," *Chaos: An Interdisciplinary Journal of Nonlinear Science*, vol. 30, no. 12, p. 123104, 2020.
- [13] A. Perinelli and L. Ricci, "Identification of suitable embedding dimensions and lags for time series generated by chaotic, finite-dimensional systems," *Phys. Rev. E*, vol. 98, p. 052226, 2018.
- [14] J. Gao and Z. Zheng, "Local exponential divergence plot and optimal embedding of a chaotic time-series," *Phys. Lett. A*, vol. 181, pp. 153–158, 1993.
- [15] M. Franchi and L. Ricci, "Statistical properties of the maximum lyapunov exponent calculated via the divergence rate method," *Phys. Rev. E*, vol. 90, p. 062920, 2014.
- [16] L. Ricci, A. Perinelli, and M. Franchi, "Asymptotic behavior of the time-dependent divergence exponent," *Phys. Rev. E*, vol. 101, p. 042211, 2020.
- [17] L. M. Pecora and T. L. Carrol, "Synchronization in chaotic systems," *Phys. Rev. Lett.*, vol. 64, no. 8, p. 821–824, 1990.
- [18] S. Boccaletti, J. Kurths, G. Osipov, D. Valladares, and C. Zhou, "The synchronization of chaotic systems," *Physics Reports*, vol. 366, no. 1, pp. 1–101, 2002.
- [19] U. Kocamaz, S. Çiçek, and Y. Uyaroglu, "Secure communication with chaos and electronic circuit design using passivity-based synchronization," *Circuits Syst Comput*, vol. 27, p. 1850057, 2018.
- [20] A. Khitun, M. Bao, J. Lee, K. Wang, D. Lee, S. Wang, and I. Roshchin, "Inductively coupled circuits with spin wave bus for information processing," *Nanoelectron Optoelectron*, vol. 3, pp. 24–34, 2008.
- [21] S. Boccaletti, A. N. Pisarchik, C. I. del Genio, and A. Amann, *Synchronization: From Coupled Systems to Complex Networks*. Cambridge University Press, 2018.
- [22] A. Uchida, M. Shinozuka, T. Ogawa, and F. Kannari, "Experiments on chaos synchronization in two separate microchip lasers," *Opt. Lett.*, vol. 24, no. 13, pp. 890–892, 1999.
- [23] T. Sugawara, M. Tachikawa, T. Tsukamoto, and T. Shimizu, "Observation of synchronization in laser chaos," *Phys. Rev. Lett.*, vol. 72, no. 22, pp. 3502–3505, 1994.
- [24] S. Sivaprakasam and K. Shore, "Demonstration of optical synchronization of chaotic external-cavity laser diodes," *Opt. Lett.*, vol. 24, no. 7, pp. 466–468, 1999.
- [25] S. Sivaprakasam and K. Shore, "Cascaded synchronization of external-cavity laser diodes," *Opt. Lett.*, vol. 26, no. 5, pp. 253–255, 2001.
- [26] M. Mehrabbeik, S. Jafari, R. Meucci, and M. Perc, "Synchronization and multistability in a network of diffusively coupled laser models," *Communications in Nonlinear Science and Numerical Simulation*, vol. 125, p. 107380, 2023.
- [27] S. Boccaletti, J. Almendral, S. Guan, I. Leyva, Z. Liu, I. Sendiña-Nadal, Z. Wang, and Y. Zou, "Explosive transitions in complex networks' structure and dynamics: Percolation and synchronization," *Physics Reports*, vol. 660, pp. 1–94, 2016. Explosive transitions in complex networks' structure and dynamics: Percolation and synchronization.

**ROBERTO CONCAS** received his B.Sc. and M.Sc. degrees in electronics engineering from University of Cagliari, Italy. With more than 15 years experience in electronic design, hardware and firmware development, he has been collaborating in different fields such as domotics, IOT, materials engineering, biotechnology, quantum technology and spectroscopy.



He has been working for Istituto Nazionale di Ricerca Metrologica (INRiM) since 2018. He is also a member of the Electronic Workshop at European laboratory for Non-Linear Spectroscopy (LENS).

**ALESSIO MONTORI** is an electronics technician with a specialization in optoelectronics. He has more than 20 years of experience in designing ultra-low noise electronics for precision spectroscopy applications.



He has been working at the National Institute of Optics (CNR) since 2012. He is involved in technology transfer and since 2022 he has held the role of CTO in ppqSense srl, a company that commercializes the first radiocarbon measurement system based on a CNR-patented spectroscopic technique.





**EUGENIO PUGLIESE** is graduated in physics and obtained his doctorate working on topics in nonlinear dynamics and complex systems. His research activity is currently focused on the development of imaging techniques for various applications. He is co-author of numerous publications both in the field of the dynamics in classical and quantum systems and in the field of optics and digital holography.



**ALESSIO PERINELLI** received the M.S. degree and Ph.D. in physics from the University of Trento, in 2017 and 2020, respectively. He is currently a Researcher at the Department of Physics of the University of Trento. His research interests concern the investigation of nonlinear and chaotic systems, the development of nonlinear time series analysis methods, and the application of nonlinear methods to signals generated by complex systems in different fields, from neuroscience to

geoscience.



**LEONARDO RICCI** (M'18) received the M.S. degree in physics from the University of Pisa, Pisa, Italy, in 1990, and the Ph.D. degree in physics from the Ludwig-Maximilian University, Munich, Germany, in 1994. From 1990 to 1994, he worked with T. W. Hänsch's Group, Munich. In 1995, he moved to the Department of Physics, University of Trento, Trento, Italy, where is currently an Associate Professor. His research interests mainly concern complex systems dynamics, entropy (in-

formation theory), and the development of nonlinear techniques for time series analysis.



**RICCARDO MEUCCI** (Senior Member, IEEE) was born in Scandicci, Firenze, Italy, in 1956. He received the Ph.D. degree in physics and the Ph.D. degree (Hons.) specialization in optics from the University of Florence, Italy, in 1982 and 1987, respectively. From 1984 to 1987, he was a Research Fellow with the Istituto di Cibernetica, National Research Council (CNR), Italy.

Since 1987, he has been with the National Institute of Optics, Firenze, Italy, where he holds the position of the Research Director. He is also a Contract Professor of physical optics and mathematical methods for optics with the University of Firenze. His research interests include nonlinear dynamics, chaos, control of chaos, synchronization, and infrared digital holography.

...